ÉCOLE POLYTECHNIQUE FÉDÉRALE DE LAUSANNE

MATHICSE

Mathematics Institute of Computational Science and Engineering

School of Basic Sciences - Section of Mathematics

MATHICSE Technical Report

Nr. 6.2012

February 2012

Three-dimensional simulation of dam break flows

Alexandre Caboussat, Sébastien Boyaval and Alexandre Masserey

http://mathicse.epfl.ch

Phone: +41 21 69 37648

Address:
EPFL - SB - MATHICSE (Bâtiment MA)
Station 8 - CH-1015 - Lausanne - Switzerland

Fax: +41 21 69 32545

Three-Dimensional Simulation of Dam Break Flows

Alexandre Caboussat [a,b] Sébastien Boyaval [c]
Alexandre Masserey [a]

[a]Ycoor Systems SA, Technopôle 10, 3960 Sierre, Switzerland

[b]Mathematics Institute of Computational Science and Engineering
Ecole Polytechnique Fédérale de Lausanne, 1015 Lausanne, Switzerland

[c]Université Paris Est, Laboratoire d'hydraulique Saint-Venant (EDF R&D – Ecole des Ponts ParisTech – CETMEF), 78401 Chatou Cedex, France ; and INRIA, MICMAC team–project, Domaine de Voluceau - Rocquencourt, B.P. 105 - 78153 Le Chesnay, France.

Abstract

A three-dimensional numerical model of free-surface hydrodynamical flows is presented for application to dam break simulations. The incompressible Navier-Stokes equations are satisfied in the water domain, while the location of the water domain is tracked as a function of time by a transport equation for an additional variable, a so-called volume-of-fluid approach. Discretization is achieved by a time splitting algorithm between the transport equations and the evolutive Stokes equations. The advection problems are solved by computing straight-line characteristics on a Cartesian grid. The diffusion problems are solved by a finite-element method on a simplicial mesh coarser than the Cartesian grid. A variety of benchmark problems illustrates the accuracy of the method when applied to dam break studies and validate the numerical approach. Numerical experiments on actual topographies illustrate the capabilities of the method, by considering in particular the Malpasset dam break test case and the (hypothetical) break of the Grande-Dixence dam in Switzerland.

Key words

Free-surface hydrodynamical flows, Volume-Of-Fluid modeling, Three-dimensional non-hydrostatic model, Dam break, Characteristics method, Finite-Element method.

1 INTRODUCTION AND MOTIVATIONS

One essential feature of dam break studies consist in accurately forecasting the fast floods that are incurred in the area (valleys) below a dam by the failure of the dam structure. The determination of the potential consequences of a dam break requires the spatial location of the flood, as well as the time evolution of the flow in terms of fronts speed and water height. Physical models have been used for a long time to predict the impacts of dam breaks, but they are costly and not always accurate enough because of the limited measurability of some quantities. Numerical models on the contrary have now proved sufficiently accurate and of reasonable cost [20] while providing physical details at any point of the flow. The goal of this article is therefore to discuss a numerical model for the simulation of dam break flows. The main characteristic of the present work is that it uses a *full three-dimensional* (3D) model, where by full we mean *non-hydrostatic* (that is, without requiring the pressure to be hydrostatic).

Several numerical models aimed at solving the so-called dam break problem are described in the literature, see, e.g., [4, 18, 19, 32]. The question of the selection of an appropriate simplified model is indeed recurrent. Full 3D models have rarely been favored due to memory and computational time requirements. Instead, the design of accurate simplified models *dedicated to the dam break problem* has been widely treated in the literature, mainly focusing on hydrostatic models [1, 19, 34] and possibly with only a one-dimensional description of the front propagation. Now, the Concerted Action on Dam Break Modelling (CADAM) project, see e.g. [18], has tackled several simplified models and has succeeded in exhibiting results of simulations that are in adequation with a number of experimental results, for instance [1].

It has recently become possible to carry out 3D numerical simulations, see e.g. [3, 9, 10, 20, 28], with a view to overcoming some of the modeling errors that necessarily arise in simplified models [23, 26, 27]. Thus, as long as they are practicable, 3D numerical simulations should now enter benchmarks, to be compared with various simplified models [16]. Furthermore, although 3D numerical simulations will remain computationally very expensive (at least for a while) and simplified models will remain useful for a number of "real-time" purposes in particular, practicable and accurate full 3D models are also desirable to help designing appropriate simplified models in specific situations that remain an actual challenge to model reduction (see Section 2 and 4.5).

In this article, we present a numerical method for the full 3D numerical simulation of dam break flows that is based on a Volume-Of-Fluid (VOF) modeling of free surfaces. The numerical method has already been used in the past for several situations where free-surface flows occur [6, 8, 25]. It is applied here

to the simulation of (i) simple dam break flows where data for approximations of the water height and mean velocity are available (either analytical expressions that are exact solutions to simplified models or well-documented numerical solutions) and (ii) real-life situations in large geometrical domains (up to 20000 [m] long). The method decouples advection and diffusion effects by an operator splitting (see [17] for instance) and invokes two different meshes (one for each fractional step). A method of characteristics on a structured grid of small cells is used for the discretization of the advection problems, without having to enforce any CFL condition (though a CFL constraint is of course theoretically required for the sake of consistency). Piecewise linear Finite-Element (FE) functions on an unstructured mesh of tetrahedrons are used for the approximation of the velocity and pressure fields as solutions to Stokes equations in the water domain.

In order to validate the numerical simulation of flooding waves with our method, benchmark problems have been considered first. The method is numerically demonstrated to converge in test cases that are exactly solvable for the well-known "one-dimensional" hydrostatic model based on Saint-Venant equations for shallow water (the Ritter test case [30] and the Stoker test case [33], where the velocity is one-dimensional in hydrostatic models). Our numerical solutions compare well with the exact solutions to the reduced shallow-water model in thin-layer regimes (when the Navier-Stokes equations formally reduce to the Saint-Venant equations) but also show some non-hydrostatic features like in [16]. We next compare with *numerical* solutions to reduced shallow-water models in a well-documented test case [4, 13, 34]. The test case consists of a simplified dam breach over a wet bed that is a 3D asymmetric extension of the Stoker test case. The numerical results allow us to assess the validity of our method for simulations in a 3D setting without symmetry.

Finally real-life examples are illustrated, namely the Malpasset dam break (see e.g. [2, 15, 18, 31]) and the hypothetical break of the Grande-Dixence dam in Switzerland. Both cases use real topologies and are computational challenges when using a 3D approach. In addition to show the capabilities of our numerical method, the simulation also shows that realistic results can be achieved with a model using as few parameters as possible: we use neither friction nor turbulence in our model.

This article is organized as follows. In the next section, the mathematical and physical models are detailed. The numerical algorithms are then briefly described. Numerical experiments are illustrated in the last section: analytical test cases first, then test cases that are numerically well-documented in the literature for simplified models, last real-life examples. The final example (Grande-Dixence dam break) illustrates the potentialities of the numerical approach in real topographies and large computational domains, in particular for policy makers to forecast floods and protect cities and inhabitants.

2 A VOF MODEL FOR 3D HYDRODYNAMICAL FREE SURFACES FLOWS

Following [25], we define $T > 0$ as the final time of simulation and consider a bounded computational domain $\Lambda \subset \mathbb{R}^3$ in which the fluid remains confined for all times $t \in [0, T]$. The domain actually occupied by the water at any given time t is denoted by $\Omega_t \subset \Lambda$ and the free surface between the water and the air by $\Gamma_t = \partial\Omega_t \backslash \partial\Lambda$. Let Q_T denote the space-time domain containing the water, that is $Q_T = \{(\mathbf{x}, t) : \mathbf{x} \in \Omega_t, 0 < t < T\}$. The velocity field $\mathbf{v} : Q_T \to \mathbb{R}^d$ and the pressure field $p : Q_T \to \mathbb{R}$ are supposed to satisfy the incompressible Navier-Stokes equations in Q_T:

$$\rho \frac{\partial \mathbf{v}}{\partial t} + \rho(\mathbf{v} \cdot \nabla)\mathbf{v} - 2\nabla \cdot (\mu \mathbf{D}(\mathbf{v})) + \nabla p = \mathbf{f}, \qquad \text{in} \quad Q_T, \tag{1}$$

$$\nabla \cdot \mathbf{v} = 0 \qquad \text{in} \quad Q_T, \tag{2}$$

where $\mathbf{D}(\mathbf{v}) = 1/2(\nabla \mathbf{v} + \nabla \mathbf{v}^T)$ is the symmetric deformation rate tensor, ρ the constant density of water, μ the constant molecular viscosity water and $\mathbf{f}$ denotes the external forces (that is the gravitational forces $\mathbf{f} = \rho \mathbf{g}$ here, with $\mathbf{g}$ the gravity). We have not used any turbulence model in our computations, though it is clearly possible to add a simple eddy viscosity at little extra-cost. At any given time t, slip or no-slip boundary conditions are enforced on the boundary of the water domain Ω_t that is in contact with the boundary of the computational domain *viz.* $\partial\Lambda \cap \partial\Omega_t$. On the water-air interface Γ_t, we require free-surface forces, that is:

$$-p\mathbf{n} + 2\mu \mathbf{D}(\mathbf{v})\mathbf{n} = 0 \qquad \text{on } \Gamma_t, \quad t \in (0, T), \tag{3}$$

where $\mathbf{n}$ is the unit normal of the water-air free surface oriented toward the air domain.

The position of the water at time t is tracked by a characteristic function $\varphi : \Lambda \times (0, T) \to \mathbb{R}$. The function φ equals one if water is present, zero if it is not. Initial conditions are given for φ to define the initial water region $\Omega_0 = \{\mathbf{x} \in \Lambda : \varphi(\mathbf{x}, 0) = 1\}$, as well as for the velocity field $\mathbf{v}$ (initially prescribed in Ω_0). The kinematics of the free surface is that of a material surface so that φ must satisfy:

$$\frac{\partial \varphi}{\partial t} + \mathbf{v} \cdot \nabla \varphi = 0 \qquad \text{in } \Lambda \times (0, T), \tag{4}$$

where $\mathbf{v}$ outside Q_T can be any continuous extension of $\mathbf{v}$ inside Q_T (see, *e.g.*, [25]). More precisely, $\mathbf{v}(\mathbf{X}(t), t) = \mathbf{v}(\mathbf{X}(0), 0)$, where $\mathbf{X}(t)$ is the trajectory of a fluid particle which is at position $\mathbf{X}(0)$ at time $t = 0$, thus $\mathbf{X}'(t) = \mathbf{v}(\mathbf{X}(t), t)$.

Last, note that it is possible to account for (i) the external pressure of the air onto the water-air interface, which is specifically useful for air bubbles trapped in the water region (see [8] for a detailed computation of the pressure in the air), and (ii) the surface tension on the water-air interface, which is specifically useful in situations where capillary effects are not negligible (unlike dam break studies, see [6]).

For future reference, we also briefly recall how (1)-(2)-(3)-(4) can be formally reduced to a shallow-water model (see e.g. [16, 24] for more details). The goal of the model reduction is to derive a closed set of equations simpler than (1)-(2)-(3)-(4) for (approximations of) $\mathbf{v}$ and φ, when the free surface is supposed to be "non-folded" over a similarly non-folded topography. That is, assuming $\Lambda = \{(x, y, z) \in S \times (0, Z)\}$ is a cylinder with base $S \subset \mathbb{R}^2$ and axis directed along the gravity, the free surface is required to be a piecewise smooth manifold with equation $z = b(x, y) + h(t, x, y)$ while $z = b(x, y)$ is the given topography equation (think of rivers and lakes.) Using scaling assumptions in a thin-layer regime with slow topography variations $|\nabla b| \ll |b|$, one can show formally that $\mathbf{v} \approx (u, v, 0)$ and $p \approx \rho g h$ where (h, u, v) satisfy the *viscous Saint-Venant* system of equations in $S \times (0, T)$:

$$\frac{\partial h}{\partial t} + \frac{\partial hu}{\partial x} + \frac{\partial hv}{\partial y} = 0, \tag{5}$$

$$h\frac{\partial u}{\partial t} + hu\frac{\partial u}{\partial x} + hv\frac{\partial u}{\partial y} + h\frac{\partial gh}{\partial x} = -h\frac{\partial gb}{\partial x} - 2\frac{\mu}{\rho}\left(\frac{\partial}{\partial x}\left(2h\frac{\partial u}{\partial x}\right) + \frac{\partial}{\partial y}\left(h\frac{\partial u}{\partial x} + h\frac{\partial u}{\partial y}\right)\right) \tag{6}$$

$$h\frac{\partial v}{\partial t} + hu\frac{\partial v}{\partial x} + hv\frac{\partial v}{\partial y} + h\frac{\partial gh}{\partial x} = -h\frac{\partial gb}{\partial x} - 2\frac{\mu}{\rho}\left(\frac{\partial}{\partial x}\left(2h\frac{\partial v}{\partial x}\right) + \frac{\partial}{\partial y}\left(h\frac{\partial v}{\partial y} + h\frac{\partial v}{\partial x}\right)\right) \tag{7}$$

Considering the smaller number of unknowns, it is computationally less costly to solve the Saint-Venant system (5)–(6)–(7) than the full 3D Navier-Stokes equations. Note that the viscous terms in (5)–(6)–(7) are very small and occur only in the "second-order" approximation to (1)–(2)–(3)–(4), but their importance arises through the determination of a unique *entropic* solution to the inviscid Saint-Venant system of balance laws obtained in the vanishing viscosity limit $\frac{\mu}{\rho} \to 0$, recall, e.g., [16, 24]. (At the numerical level, one can either solves a variational formulation of (5)–(6)–(7) like [20], or more commonly capture entropic solutions to the inviscid limit of (5)–(6)–(7) and next add viscous perturbations like, e.g., [31].)

Notice that it is also possible to include capillary effects in (5)–(6)–(7), as well as friction laws at the bottom topography. The main limitations of the reduced model are (i) a hydrostatic pressure, which is consistent with small vertical velocities and a horizontal motion "by slices" (where a given velocity profile is imposed all along horizontal directions), and (ii) a parametrized description of the free surface, which is consistent with a non-breaking flow at-

tached to the topography. The latter assumptions are not necessarily satisfied by solutions to the full 3D Navier-Stokes equations with a free surface, in particular when the bottom topography b varies fast. Non-hydrostatic corrections to (5)–(6)–(7) are difficult and cumbersome, see, e.g., [5]. But of course, those assumptions are satisfied in a number of situations (applied to geophysical flows in particular) and the shallow-water reduced model has proved useful to many applications in hydraulics (recall the discussion about dam break flows in introductory Section 1). We thus insist on the fact that, beyond benchmarking purposes, our motivations for a full 3D modeling of dam break flows are specific situations where the Saint-Venant assumptions are not satisfied (with a non-hydrostatic pressure for instance, see also Section 4.5).

3 NUMERICAL DISCRETIZATION FOR EFFICIENT 3D SIMULATIONS

The advocated numerical algorithm relies on a *time splitting method* to decouple advection and diffusion phenomena and a *two-grid approach* for the space discretization.

Let $\tau > 0$ be a given time step and $t^n = n\tau$, $n \geq 0$, be a sequence of discrete times. Let φ^n, $\mathbf{v}^n$, Ω^n be approximations of φ, $\mathbf{v}$, Ω respectively at time t^n. The approximations φ^{n+1}, $\mathbf{v}^{n+1}$, Ω^{n+1} at time t^{n+1} are computed by a splitting algorithm illustrated in Figure 1.

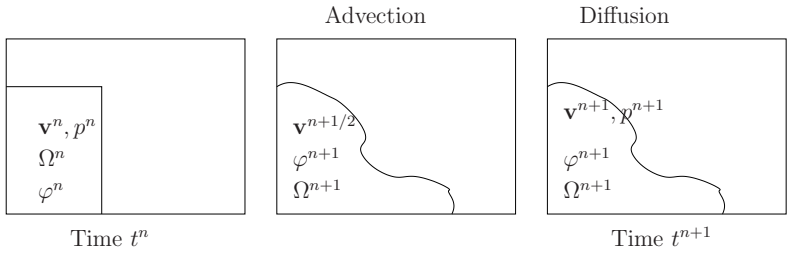

Fig. 1. The splitting algorithm (from left to right). Two advection problems are solved to determine the new approximation of the characteristic function φ^{n+1}, the new liquid domain Ω^{n+1} and the predicted velocity $\mathbf{v}^{n+1/2}$. Then, a time dependent Stokes problem is solved to obtain the velocity $\mathbf{v}^{n+1}$ and the pressure p^{n+1} in the new liquid domain Ω^{n+1}.

First two advection problems are solved, that lead to the new approximation of the characteristic function φ^{n+1} together with a prediction $\mathbf{v}^{n+1/2}$ of the new velocity in the new water domain Ω^{n+1} with free surface Γ^{n+1}. (The domain Ω^{n+1} is defined as the set of points such that φ^{n+1} equals one.) This advection step consists in solving, with an (explicit) forward characteristics method, four

transport equations between t^n and t^{n+1}:

$$\frac{\partial \varphi}{\partial t} + \mathbf{v} \cdot \nabla \varphi = 0, \qquad \frac{\partial \mathbf{v}}{\partial t} + (\mathbf{v} \cdot \nabla)\mathbf{v} = 0, \tag{8}$$

with initial conditions given by the values of the functions φ and $\mathbf{v}$ at time t^n. The solutions read $\varphi^{n+1}(\mathbf{x}+\tau\mathbf{v}^n(\mathbf{x})) = \varphi^n(\mathbf{x})$ and $\mathbf{v}^{n+1/2}(\mathbf{x}+\tau\mathbf{v}^n(\mathbf{x})) = \mathbf{v}^n(\mathbf{x})$ for all $\mathbf{x} \in \Omega^n$.

Then, a time dependent Stokes problem is solved in $\Omega^{n+1} \times (t^n, t^{n+1})$ using the predicted velocity $\mathbf{v}^{n+1/2}$ as initial condition. We use an (implicit) backward Euler scheme. The velocity $\mathbf{v}^{n+1}$ and the pressure p^{n+1} are thus solution to a boundary value problem:

$$\begin{aligned} &\rho \frac{\mathbf{v}^{n+1} - \mathbf{v}^{n+1/2}}{\tau} - 2\nabla \cdot \Big(\mu \mathbf{D}(\mathbf{v}^{n+1})\Big) + \nabla p^{n+1} = \mathbf{f}^{n+1} \quad \text{in } \Omega^{n+1}, \\ &\nabla \cdot \mathbf{v}^{n+1} = 0 \quad \text{in } \Omega^{n+1}, \end{aligned} \tag{9}$$

with boundary condition (4) on Γ^{n+1} and slip or no-slip elsewhere (recall Section 2).

Two different spatial discretizations are used for the advection problems and for the Stokes problem, as illustrated in Figure 2. A regular grid of square cells $\mathcal{C}_h$ is used to solve the advection problems, while the Stokes problem is solved on a coarser unstructured tetrahedral finite element mesh $\mathcal{T}_H$.

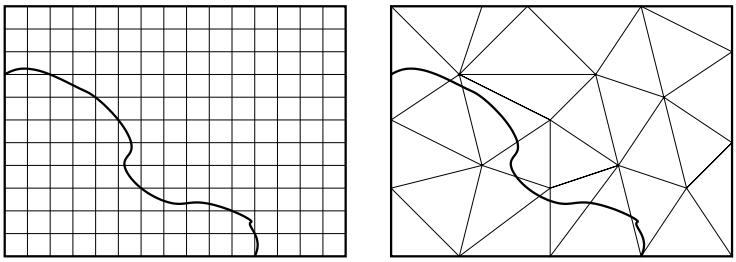

Fig. 2. Two-grid method in the two-dimensional case: structured grid of small square cells $\mathcal{C}_h$ (left) and unstructured finite element mesh of triangles $\mathcal{T}_H$ (right).

3.1 Advection Step

The cavity Λ is embedded into a box that is meshed into a structured grid denoted by $\mathcal{C}_h$, made of cubic cells of size h. We label each cell C_{ijk} by the multi-index (ijk), where the indices i, j, k vary respectively only in each one of the three spatial directions of a Cartesian frame. All advection steps are solved on the same structured grid $\mathcal{C}_h$ with a forward characteristics method detailed

in [25], using, at any time t^n, piecewise constant approximations of φ^n and $\mathbf{v}^n$ on $\mathcal{C}_h$ (hence a collection of values φ^n_{ijk}, $\mathbf{v}^n_{ijk}$ indexed by their cell label (ijk)). The algorithm consists in moving the cell (ijk) in the direction $\tau\mathbf{v}^n_{ijk}$ and next conservatively distributing the transported quantities φ^n_{ijk} and $\mathbf{v}^n_{ijk}$ into the overlapped cells (with ratio the area intersected by the transported cell divided by the area of the transported cell). Yet, the repeated projection of a cell onto the structured grid is an overly diffusive procedure for accurate propagation of a front like Γ^n. We use a variation of the heuristic SLIC algorithm [25] to reduce the numerical diffusion of the front. The cells where $\varphi^n_{ijk} = 0$ or 1 are treated first. Next, in the cells (ijk) where $0 < \varphi^n_{ijk} < 1$, a square subcell is defined within (ijk), with center such that some of its edges coincide with an edge of the cell (ijk), on the other side of which the approximation of φ^n is also non-uniformly 0, if possible. The subsequent translation and the projection of those latter subcells follow the same rule as before. Last, to avoid $\varphi^{n+1}_{ijk} > 1$ for some (ijk), a post-processing technique redistributes the excess of water from over-filled cells to cells (ijk) where $0 < \varphi^n_{ijk} < 1$. In most computations, we could check that only a very small amount of excess water cannot be redistributed (the so-called numerical compression, see [25]).

3.2 Diffusion Step

Let $\mathcal{T}_H$ be a tetrahedral discretization of the cavity Λ satisfying the usual compatibility conditions between tetrahedra to define a FE mesh (see e.g. [17]). The maximal diameter of the elements is denoted by H (typically $H \simeq 5h - 10h$). We denote by P_ℓ the nodes of the FE mesh.

Once values φ^{n+1}_{ijk} and $\mathbf{v}^{n+1/2}_{ijk}$ have been computed on $\mathcal{C}_h$, one computes continuous piecewise linear approximations of φ^{n+1}_H and $\mathbf{v}^{n+1/2}_H$ on $\mathcal{T}_H$ by assigning to each degree of freedom P_ℓ an average value in a patch of neighboring cells (a local L^2-projection with mass lumping):

$$\varphi^{n+1}_{P_\ell} = \sum_{K,\, P_\ell \in K} \sum_{ijk,\, C_{ijk} \in K} \left(\frac{\psi_{P_\ell}(C_{ijk})}{\displaystyle\sum_{K,\, P_\ell \in K} \sum_{ijk,\, C_{ijk} \in K} \psi_{P_\ell}(C_{ijk})} \right) \varphi^{n+1}_{ijk},$$

where ψ_{P_ℓ}, $j = 1, \ldots, N$ denotes the continuous piecewise linear functions defining a FE basis with non-zero value only at node P_ℓ.

We denote by Ω^{n+1}_H the approximation of the water domain Ω^{n+1} defined as the union of all elements of the finite element mesh such that one of their vertices P has a value $\varphi^{n+1}_P > 0.5$, and by Γ^{n+1}_H the approximation of the water-air interface Γ^{n+1}, thus an error of order $\mathcal{O}(H)$ (an adaptive mesh algorithm for the improvement of that projection error has been discussed in [7].)

Let us denote by $\mathbf{v}_H^{n+1}$ (resp. p_H^{n+1}) the piecewise linear approximation of $\mathbf{v}^{n+1}$ (resp. p^{n+1}). The Stokes problem is solved with a stabilized discrete variational formulation (Galerkin Least Squares method) and consists in finding the velocity $\mathbf{v}_H^{n+1}$ and pressure p_H^{n+1} such that:

$$\begin{aligned}
&\int_{\Omega_H^{n+1}} \frac{\mathbf{v}_H^{n+1} - \mathbf{v}_H^{n+1/2}}{\tau} \mathbf{w} d\mathbf{x} + 2\mu \int_{\Omega_H^{n+1}} \mathbf{D}(\mathbf{v}_H^{n+1}) : \mathbf{D}(\mathbf{w}) d\mathbf{x} - \int_{\Omega_H^{n+1}} \mathbf{f}\mathbf{w} d\mathbf{x} \\
&- \int_{\Omega_H^{n+1}} p_H^{n+1} \nabla \cdot \mathbf{w} d\mathbf{x} - \int_{\Omega_H^{n+1}} q \nabla \cdot \mathbf{v}_H^{n+1} q d\mathbf{x} \\
&- \sum_{K \subset \Omega_H^{n+1}} \alpha_K \int_K \left(\frac{\mathbf{v}_H^{n+1} - \mathbf{v}_H^{n+1/2}}{\tau} + \nabla p_H^{n+1} - \mathbf{f}^{n+1} \right) \cdot \nabla q d\mathbf{x} = 0, \qquad (10)
\end{aligned}$$

for all $\mathbf{w}$ and q, the velocity and pressure test functions compatible with the boundary conditions on $\partial\Lambda$. The value of the stabilization parameter α_K (a function of the local Reynolds number) has been discussed in [25]. The corresponding linear system is solved with a standard GMRES method without restarting technique (from the library SparseLib++), with an ILU preconditioner.

The continuous piecewise linear approximation of the velocity $\mathbf{v}_H^{n+1}$ on $\mathcal{T}_H$ is finally restricted at the center of each cell C_{ijk} to obtain the values $\mathbf{v}_{ijk}^{n+1}$ on the structured grid $\mathcal{C}_h$ for the next advection step. When C_{ijk} belongs to the element K, the new velocity is given by the linear interpolation $\mathbf{v}_{ijk}^{n+1} = \sum_{P_\ell \in K} \mathbf{v}_{P_\ell}^{n+1} \psi_{P_\ell}(C_{ijk})$.

4 NUMERICAL EXPERIMENTS

The results of several numerical experiments are presented in this section. In order to demonstrate the validity of the proposed numerical method in the particular framework of dam break flows, we first benchmark the numerical approach by using well-documented examples. The first step of the validation process is a comparison with analytical formulas [22, 29, 32]. We present here the classical Ritter [30] and Stoker [33] test cases, when a *one-dimensional* dam breaks over a dry or wet bed respectively. In those cases, the water level and the depth-averaged velocity solution to the Navier-Stokes equations are well approximated by the solution to the simplified 1D model for shallow-water flows, the Saint-Venant equations (5)–(6)–(7), which have explicit analytical formulas here. In a second step, comparison with well-documented examples are presented (asymmetric dam, Malpasset dam break), which allow to validate our approach for the capture of water waves in complex settings. We end this section with the new real-life simulation of the (hypothetical) break of a

large dam in Switzerland. All computations in this Section are achieved on an Intel Xeon (2.93GHz) with 8GB memory.

4.1 The Analytical Ritter Test Case

The Ritter test case considers a 1D channel with a flat horizontal bottom (which we orient toward x). The dam is vertical and breaks instantaneously at initial time. The initial conditions for the water height are:

$$h_0(x) = \begin{cases} h_0, \; x < a, \\ 0, \quad x \geq a. \end{cases} \tag{11}$$

with zero initial velocity; h_0 is the initial height of the water and a is the initial location of the dam. Relationship (11) implies that, downstream of the dam, the domain is assumed to be *dry*, while the fluid upstream is initially at rest. This is a simple Riemann problem for the Saint-Venant equations and their exact solution is made of one rarefaction wave, see, e.g., [11]:

$$h(x,t) = \frac{\left(2\sqrt{||\mathbf{g}||_2\, h_0} - \dfrac{x-a}{t}\right)}{9\,||\mathbf{g}||_2}, \qquad u(x,t) = \frac{2}{3}\left(\sqrt{||\mathbf{g}||_2\, h_0} + \frac{x-a}{t}\right), \tag{12}$$

if $-1 < x/(t\sqrt{||\mathbf{g}||_2\, h_0}) < 2$ (elsewhere, the solution is equal to the initial condition). Numerical simulations can be done using Navier-stokes equations and a three-dimensional velocity in the same setting after extruding the computational domain into a transverse direction (hence in a channel with a rectangular cross-section). The profile of the water-air interface is then compared to (12).

Let us consider the geometry described in [16], namely the channel defined by the domain $(-50, 50)\times(0, 2)\times(0, 3)$. The initial height is $h_0 = 2$ and the dam is initially located at abscissa $a = 0$. The liquid properties are $\mu = 10^{-3}$ [kg/(ms)] and $\rho = 10^3$ [kg/m^3] (water). Surface tension is neglected and slip boundary conditions are imposed at the bottom of the channel. Figure 3 visualizes the profile (water height) of the numerical solution for several mesh sizes (coarse to fine) and its comparison with (12) at times $t = 0, 3$ and 5 [s]. It is visualized on the fine grid of small cells $\mathcal{C}_h$; the time step is decreased accordingly to the mesh sizes. The corresponding CFL condition is between 2 for the coarse mesh and 0.8 for the finer mesh, guaranteeing that the CFL is smaller than one at the limit.

One can see that the numerical approximations converge and the free surface solution to the full three-dimensional Navier-Stokes equations is actually

closed to the water front predicted by the Saint-Venant equations, like in [12]. However, there is a difference between the Navier-Stokes and the Saint-Venant predictions that is localized close to the front advancing in the vacuum. There, the front speed seems smaller in the Navier-Stokes than in the Saint-Venant predictions. This little effect on the free surface close to the yet dry bottom decreases but does not seem to completely vanish as the discretization parameters are refined. (Recall that the results in Figure 3 are shown on the grid $\mathcal{C}_h$, but the velocity is approximated on a coarser mesh $\mathcal{T}_H$ that is refined similarly.) The question thus arises whether this effect is a purely numerical artefact, maybe inherent to 3D numerical simulations where the velocity is not constant along a vertical slice but also discretized (in contrast with shallow-water models), or whether it is a manifestation of non-hydrostatic effects in a full 3D modelling (when the water velocity varies fast along the direction where the water front propagates, the Navier-Stokes pressure cannot be hydrostatic). Figure 4 actually shows that the approximation of the velocity converges when the mesh size and time step tend to zero. Moreover there is a non-zero vertical component of the velocity suggesting a manifestation of non-hydrostatic effects localized more precisely at the advancing front but it is not very significant.

Concerning the computational cost and time, numerical simulations take approximately 10 minutes on the coarse mesh, approx. 50 minutes on the middle mesh, and approx. 12 hours on the fine mesh. As the mesh size is divided approximately by two in each directions, and the time step is also divided by two, one can see that the numerical algorithms scale appropriately (approximately 12 times longer for a problem 16 times larger).

4.2 The Analytical Stoker Test Case

In the case of the Stoker test case, the water released as the dam breaks flows over a *wet bed* instead of a *dry bed*. We consider the same channel and the same physical properties for the fluid as in the previous section, but the initial conditions are

$$h_0(x) = \begin{cases} h_l, \ x < a, \\ h_r, \ x \geq a. \end{cases} \tag{13}$$

for the water height, together with zero initial velocity; h_l and h_r are the initial heights of the water on the left and right sides of the dam, and a is the initial location of the dam on the Ox direction. In the Stoker case, the exact solution to Saint-Venant equations is the superimposition of two waves (see, e.g., [20]): one up-going rarefaction wave and one down-going shock wave connected by a

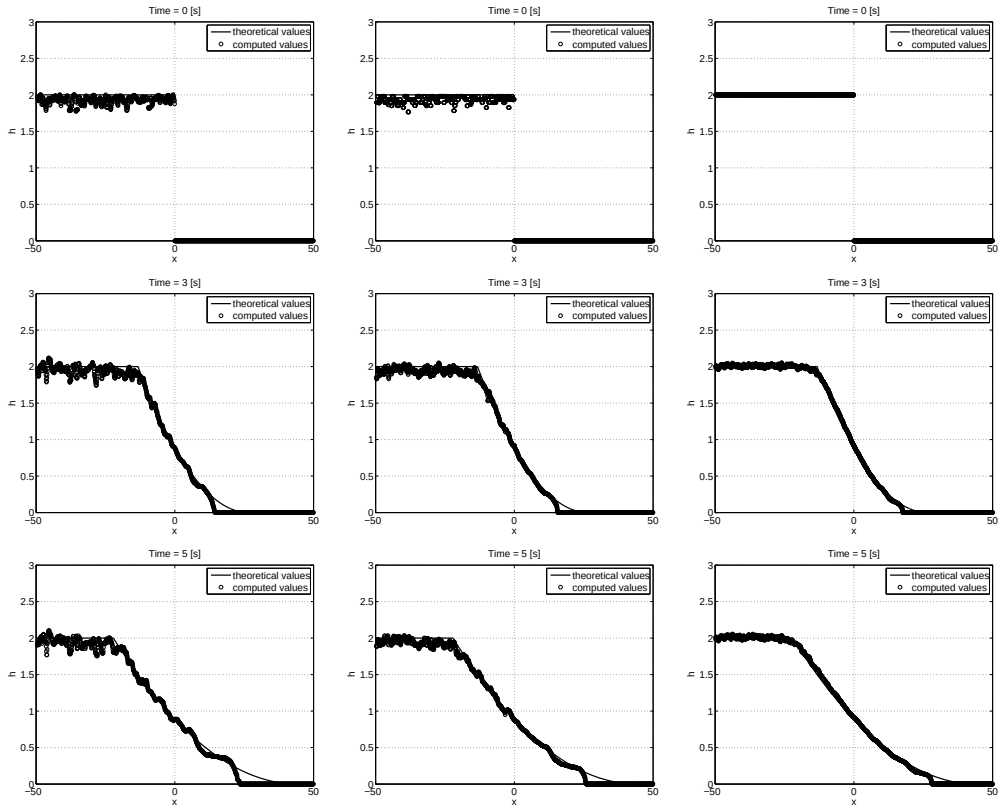

Fig. 3. Ritter analytical test case: comparison with analytical solution at times $t = 0, 3$ and 5 [s]. Left: coarse mesh ($h = 8 \cdot 10^{-2}, H = 3/5, \tau = 0.1$); middle: middle mesh ($h = 6 \cdot 10^{-2}, H = 3/8, \tau = 0.05$); right: fine mesh ($h = 4 \cdot 10^{-2}, H = 3/14, \tau = 0.025$). All the grid points on the free surface are represented, including those in the transverse direction.

medial zone with a constant depth h_m and constant velocity u_m. Let us define $c_l = \sqrt{||\mathbf{g}||_2 \, h_l}$, $c_r = \sqrt{||\mathbf{g}||_2 \, h_r}$ and $c_m = \sqrt{||\mathbf{g}||_2 \, h_m}$, then analytical formulas read, when $a = 0$,

$$h(x,t) = \begin{cases} h_l & \text{if } x < -c_l t, \\ \dfrac{\left(2\sqrt{||\mathbf{g}||_2 h_l} - \dfrac{x}{t}\right)}{9||\mathbf{g}||_2}, & \text{if } -c_l t < x < (u_m - c_m)t, \\ h_m & \text{if } (u_m - c_m)t < x < Wt, \\ h_d & \text{if } Wt < x, \end{cases} \tag{14}$$

where W is the speed of the hydraulic jump given by the Rankine-Hugoniot relation as $W = \dfrac{h_m u_m}{h_m - h_r}$. They can be made explicit by computing h_m and u_m through the conservation of invariants across the waves.

Let us consider initial heights given by $h_l = 2$ and $h_r = 1$. Figure 5 visualizes

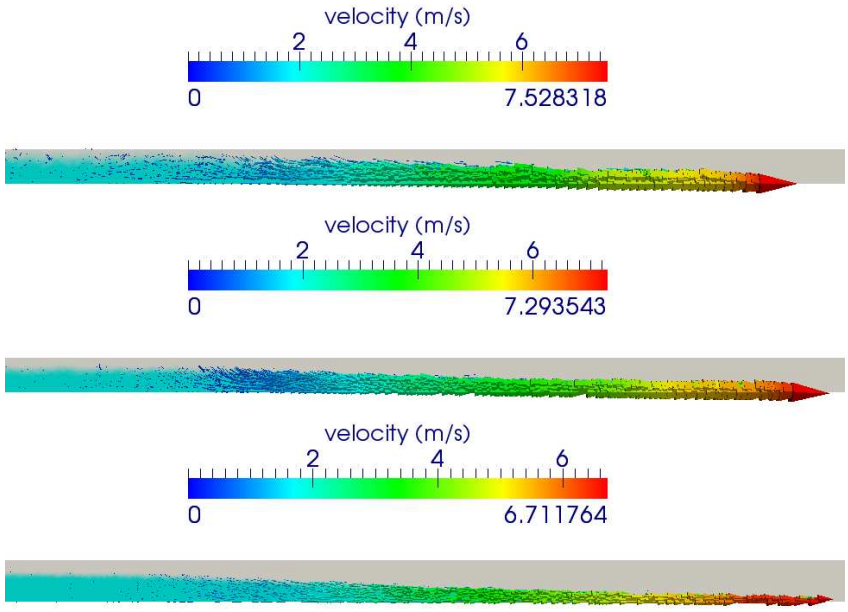

Fig. 4. Ritter analytical test case: Visualization of the velocities at time $t = 5$ [s]. Top: coarse mesh; middle: middle mesh; bottom: fine mesh.

the profile of the numerical solution, computed on the fine grid of small cells $\mathcal{C}_h$ and its comparison with (14) at times $t = 0, 3$ and 5 [s]. Three mesh sizes and time steps are considered, leading to CFL number between 2 for coarse meshes and 0.9 for fine meshes, guaranteeing that the CFL is smaller than one for fine meshes. Numerical results show good agreement between the theoretical and approximated solutions: the approximation near the shock release is accurate and converges with the time step and mesh size. Convergence of the water heights is obtained when the mesh sizes and time steps tend to zero, and numerical results compare well with [16]. Compared with the exact Saint-Venant solution, an overshoot occurs around the shock wave together with an oscillation close to the rarefaction wave in a similar fashion as in [16] for full 3D Navier-Stokes model. These features do not completely vanish as the discretization parameters are refined and seem clearly due to non-hydrostatic effects that are accounted for only by the full 3D Navier-Stokes model. Figure 6 actually shows that the approximation of the velocity converges when the mesh size and time step tend to zero. Moreover it includes a significant non-zero vertical component (compared for instance with the Ritter test case), suggesting a manifestation of non-hydrostatic effects localized more precisely at the advancing front. We note in passing that the numerical method we used here to discretize the full 3D Navier-Stokes model is quite different from that in [16].

In order to emphasize the three-dimensional character of the computational solver, let us extend this Stoker test case to a full three-dimensional situation, following [1, 21]. This example allows to check the preservation of the sym-

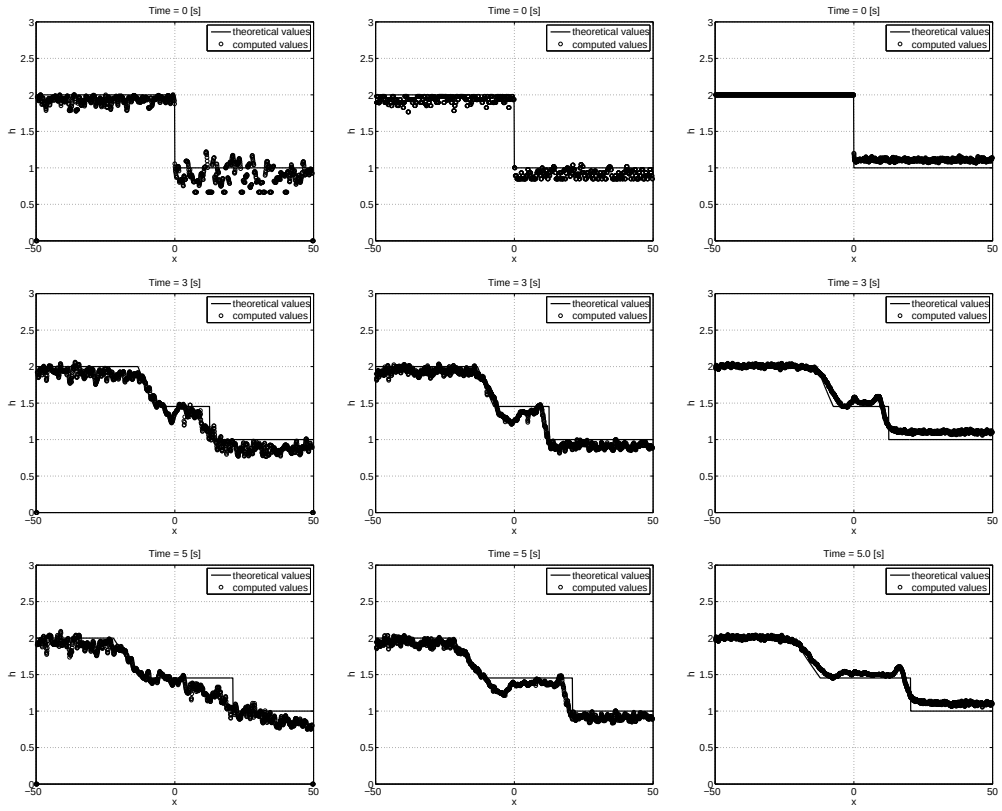

Fig. 5. Stoker analytical test case: comparison with analytical solution at times $t = 0, 3$ and 5 [s]. Left: coarse mesh ($h = 8 \cdot 10^{-2}, H = 3/5, \tau = 0.1$); right: middle mesh ($h = 6 \cdot 10^{-2}, H = 3/8, \tau = 0.05$); right: fine mesh ($h = 4 \cdot 10^{-2}, H = 3/14, \tau = 0.025$). All the grid points on the free surface are represented, including those in the transverse direction.

metry of the solution, even though the advection operator is solved on the structured grid of cells $\mathcal{C}_h$ that is aligned with the coordinates axes.

The dimensions of the computational domain are $20 \times 20 \times 3$ [m^3]. A cylindrical column of water of height $w_l = 2.5$ [m] and radius $r = 2.5$ [m] is initially located at the center of the domain. The rest of the domain is filled (wet bed) with water up to an height of $w_r = 0.5$ [m]. The column of water is released at time $t = 0$ [s].

The finite element mesh $\mathcal{T}_H$ contains 1323720 elements, which corresponds to $H = 0.1$ [m]. The size of the cells in $\mathcal{C}_h$ is $h = 0.01$ [m]. The time step is $\tau = 0.01$ [s]. Figure 7 shows the magnitude of the water velocity field at different times. The radial invariance of the front is well-preserved.

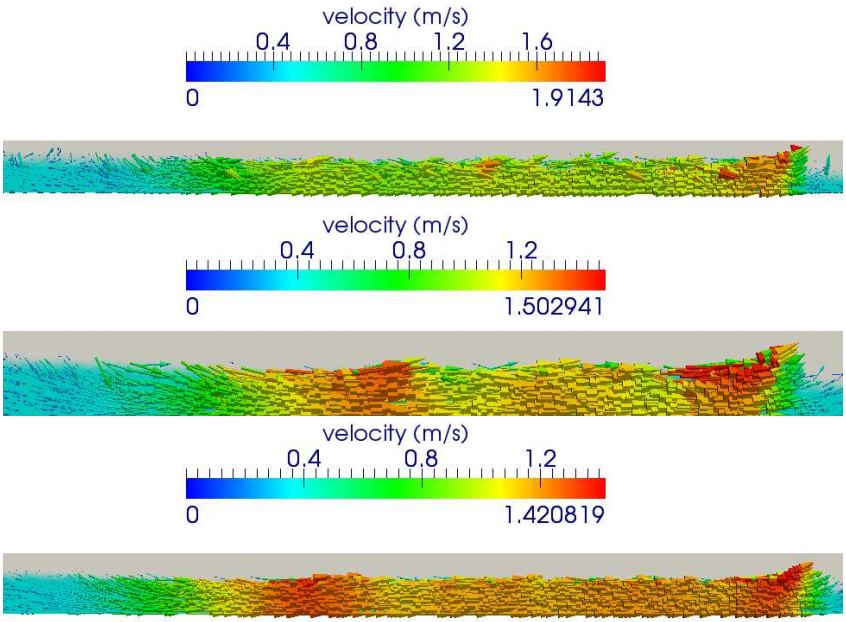

Fig. 6. Stoker analytical test case: Visualization of the velocities at time $t = 5$ [s]. Top: coarse mesh; middle: middle mesh; bottom: fine mesh.

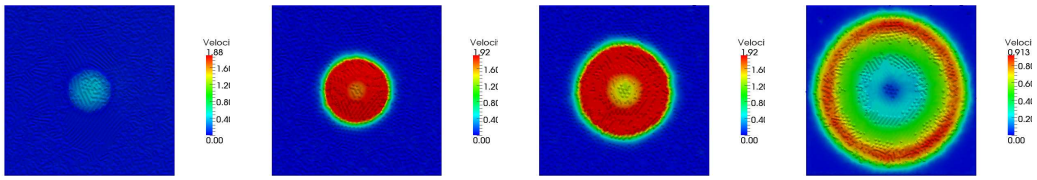

Fig. 7. Axisymmetric Stoker test case: visualization of the velocity magnitude of the water surface at times $0, 0.5, 1.0$ and 2.5 [s] (left to right).

4.3 Partial dam break (or dam breach) over a flat wet bed

This benchmark problem is a popular test case of a dam break over a wet bed [4, 13, 34]. The dam is partially, instantaneously, broken at time $t = 0$ [s], in an asymmetric manner, as only a non-central part of the dam is removed – the dam breach.

The computational domain is constructed by vertical extrusion on 20 [m] of a 2D unstructured mesh of the domain $(0, 200) \times (0, 200)$ [m^2]. Specific dimensions of the dam can be found, e.g., in [4]. The 3D finite element mesh is composed of 567364 elements and 97146 vertices, for a mesh size $H \simeq 2$ [m]. The size of the small structured grid of cells is $h = 0.5$ [m]. The time step is $\tau = 0.05$ [s], implying that the CFL number is close to 0.5. While slip boundary conditions are still enforced on the lateral walls, we imposed no-slip boundary conditions on the (flat) bottom for this test case, in contrast with the two previous test cases where slip boundary conditions were used. Note that slip and no-slip boundary conditions are the two limits between which

the whole range of boundary conditions with a friction term like Manning in shallow-water models varies. The location of the liquid at initial time consists of two layers of water at rest (zero initial velocity) with respective heights of $h_1 = 10$ [m] (on the left side of the dam) and $h_2 = 5$ [m] (on the right side of the dam). At time $t = 0$ [s], the non-central part of the dam is removed.

Figure 8 visualizes the water height at times $t = 0.05, 2.55, 5.05$ and 7.55 [s]. Results can be easily compared with those of the literature (in particular in [4, 13] and references therein). One can observe that the shape of the contours are very comparable to the existing results of the literature, while the amount of the overshoot of the advancing front is slightly reduced. While the presence of an overshoot at the front is again a manifestation of non-hydrostatic effects, it is significantly reduced here, probably due to the modeling (no-slip boundary conditions) and numerical artifacts inherent to 3D methods (3D diffusion, maybe further increased here because of the coarse character of the mesh we use for efficient 3D velocity approximations).

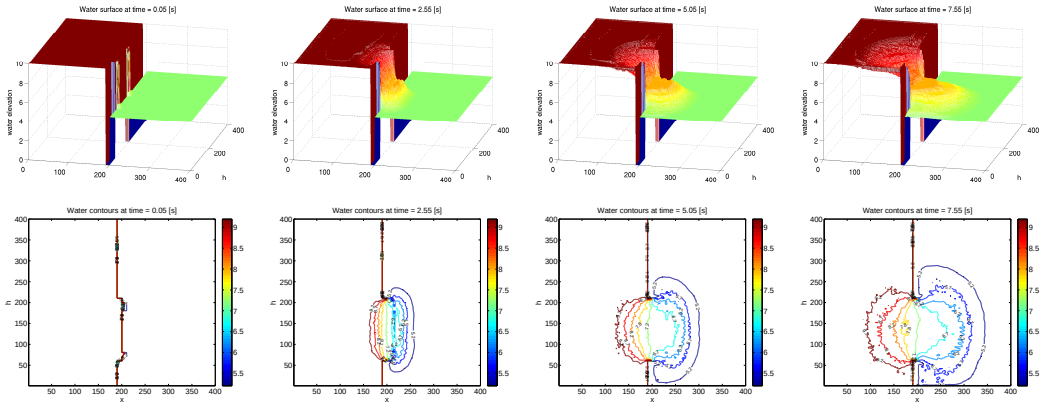

Fig. 8. Partial dam break over a flat wet bed at times $t = 0.05, 2.55, 5.05$ and 7.55 [s]. Top: water height (in meters); bottom: contours of water height (in meters).

4.4 Malpasset dam break

The Malpasset dam was located in a narrow gorge of the Reyran river valley, approximately 12000 [m] upstream of Frejus on the French Riviera. The maximum reservoir capacity was meant to be 55106 [m^3]. The dam failed explosively on December 2, 1959. The flood wave ran along the Reyran valley to Frejus. The evolution of the water front and water height has been well-documented via data collection and measurement, or reproduction with a physical model.

The test case of the breakage of the Malpasset dam has been widely treated in the literature, see, e.g., [2, 14, 18, 19]. This test case has also been a benchmark model for *Electricité de France (EDF)* for several years, in order to validate simplified 1D or 2D models based on shallow water equations. 3D simulations

of the Malpasset dam break are less frequent and can be found, for instance, in [3, 20]. The purpose of treating the Malpasset situation here is two-fold: first, it allows to compare a full 3D model with a minimum number of parameters to simplified 1D or 2D models; second, it allows to discuss fine features of the flow such as non-hydrostatic effects in the presence of a non-trivial topography. Finally, this section also shows the feasibility of such large-scale simulation. To the best of our knowledge, only qualitative results of the Malpasset dam break have been presented when using numerical simulation in three dimensions. Here, we aim at quantifying some effects of the three-dimensional approach.

The 3D computational domain is constructed by extrusion. The 2D map of the topography has been digitized from ancient topographical maps (see [18] and references therein). The overall dimensions of the domain are 17500 [m] $\times$ 9000 [m]. Elevation of the valley ranges from -20 [m] (below sea level) to $+100$ [m] (above sea level); this latter value is an estimation of the initial free surface elevation in the reservoir. The 2D mesh contains 13541 points and 39541 triangles. It is illustrated in Figure 9 (left), as actually available in the public domain. This mesh is then extruded over 10 layers of prisms, each of them cut into six tetrahedra, to form a 3D finite element mesh $\mathcal{T}_h$ of 311443 vertices and 1716000 elements. The cell size of the structured mesh is $h = 2$ [m].

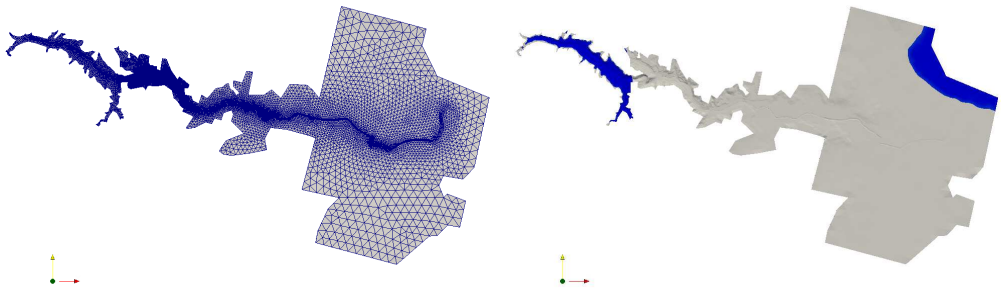

Fig. 9. Malpasset test case: Two-dimensional mesh of the topography (left) and initial position of the liquid – the lake behind the dam and the sea – (right).

The dam structure is following a straight line between the points of (X, Y) coordinates: $(4701.18\ [\mathrm{m}], 4143.41\ [\mathrm{m}])$ and $(4655.5\ [\mathrm{m}], 4392.10\ [\mathrm{m}])$. The reservoir level is located behind the dam, at a constant water level equal to 100 [m]. The level of the Mediterranean sea is constant and equal to zero. Initial conditions are also represented in Figure 9 (right). The remaining part of the bottom of the domain is dry. At time $t = 0$, the dam is completely and instantaneously removed; the water therefore flows down the valley. The value of the inlet discharge is set to zero, although this value is not known exactly. No-slip boundary conditions are enforced on the bottom topography (unlike published results we do not calibrate any friction coefficient).

Data being available, both as measurements or bench simulations on a reduced-scale model, they can be compared with the numerical results. Indeed, electric transformers have been shut down by the flood, giving a good estimate of the height and arrival time of the water at certain given points. Moreover, several points of given coordinates have been measured by the police to determine the water height. Finally, nine points (*gauge points*) have been measured thanks to a reduced-scale physical model. The coordinates of these particular points can be found, e.g. in [18, 20]. We base the comparisons on the gauge points in the present section.

Figure 10 shows snapshots of the solution at times $t = 0, 100, 200, 300, 400$ and 500 [s], together with a visualization of the velocity field. Each time step, corresponding to one second of simulation, takes approx. 12 minutes of CPU time (inputs and outputs not included).

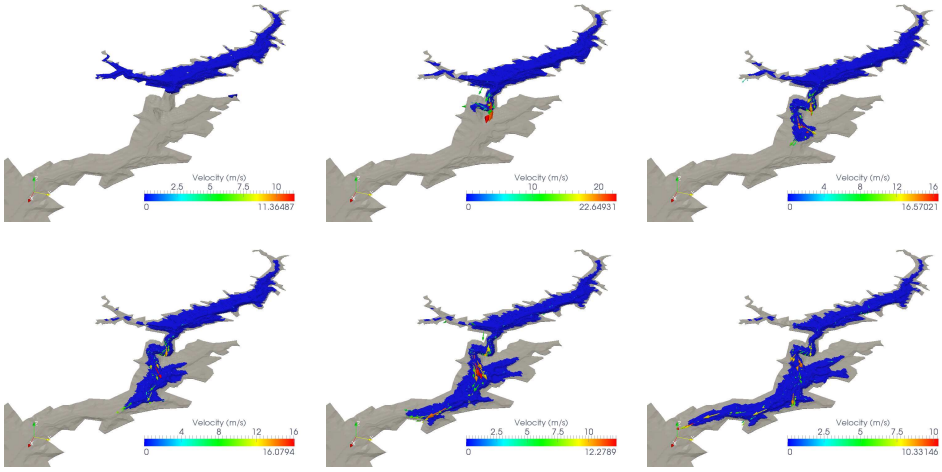

Fig. 10. Malpasset dam break: snapshots of the 3D solution at times $t = 0, 100, 200, 300, 400$ and 500 [s].

Figure 11 shows a comparison between the numerical results and physical results obtained with the reduced scale model. The comparison focuses on the maximal water height (left) and the arrival time of the first water wave (right) at the *gauge points*. Figure 11 (right) shows that the computed arrival times of the water wave at these given points is larger than the ones of the physical model. This means that the wave calculated with the 3D numerical simulation actually travels slowlier than the physical one. This is not surprising and is a consequence of i) the inherent numerical diffusion of a three-dimensional model due to a relatively large mesh size; ii) the no-slip boundary conditions on the topography that slow the water evolution.

On the other hand, Figure 11 (left) show the maximal water level at these gauge points. We observe that numerical results are quite oscillatory. These oscillations may be coming from various sources, among them increased numerical approximations in 3D simulations. But in view of the results in Figure 5

for the Stoker test case, we believe they mostly originate in overshoots at the forefront of a shock wave.

These overshoots may be amplified by the numerical scheme. But they are inherent to the non-hydrostatic character of the model. The water level evolution at some of the gauge points (markers 3,5, and 6) is shown in Figure 12. One can see there that overshoots happen only on one time step, that is seemingly at the arrival of a shock wave (primary or secondary, because of flood reflections in branches of the submerged valley), and especially for the gauge points 3 and 5 where the maximum water level is overestimated by our model compared with the physical model. Numerical results are smoother and more accurate in regions with a smoother topography (e.g. gauge marker 6). And one can explain why overshoots are especially strong at the gauge points 3 and 5; indeed (i) the gauge markers 3 and 5 are physically located at the intersection of valleys where interacting waves may amplify the shock, and (ii) the topography varies quite fast below these points and induces non-hydrostatic effects.

We smooth the numerical results to better compare with hydrostatic models. (Physical measurements would also be smoothed by any device that need a minimal time range for data acquisition.) Figure 11 shows that the post-processed numerical results match more accurately the maximum water level, without changing the arrival times.

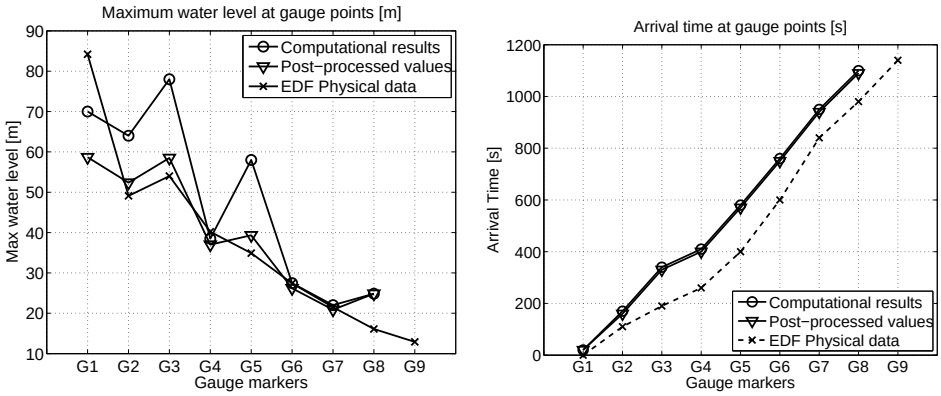

Fig. 11. Malpasset dam break: maximum water level and wave arrival times at the gauge points. Comparison between numerical results and results from the reduced-scale physical model.

4.5 Dam of Grande-Dixence

The last numerical experiment tackles the hypothetical dam break of the Grande-Dixence dam located in Switzerland, and the resulting flooding of the valley *Val d'Hérens*. The Grande-Dixence dam is the tallest dam in Switzer-

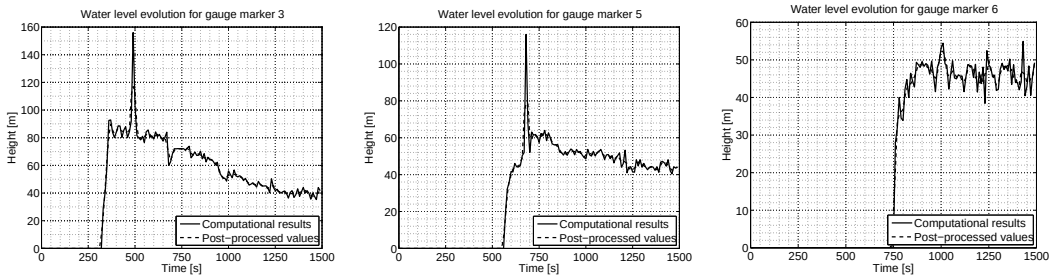

Fig. 12. Malpasset dam break: water level evolution at the gauge markers 3, 5 and 6. Computational results and post-processed values.

land. Opened in 1965, it is 285 [m] high and the lake created behind the dam (*Lac des Dix*) contains 400 [mio m^3] of water. It is located at the top of a 30000 [m] long valley leading to the river Rhone and directly above the city of Sion.

The computational domain is constructed as follows. A two-dimensional elevation map is obtained from Swiss topographical data. The resolution of the structured two-dimensional mesh is 25 [m]. The 3D finite element mesh is generated by extrusion of the 2D map on 10 layers of prisms, split into six tetrahedra each, leading to a finite element mesh composed of 13876525 elements and 2057005 vertices with resolution $H = 50$ [m]. The computational domain is thus 5750 [m] wide, 28900 [m] long and 400 [m] high. On the other hand, the structured grid of small cells has a resolution of $h = 10$ [m]. No-slip boundary conditions are imposed on the bottom topography. The dam of height 285 [m] is initially assumed filled with 400 [mio m^3] of water at rest.

Figure 13 illustrates the location of the liquid front at several times of the simulation and the flooding areas in the valley. Figure 14 illustrates snapshots of the water domain colored according to the instantaneous liquid velocity, which ranges from 0 to 120 [m/s]. Finally, Figure 15 illustrates the water height at several time steps. The water height ranges from 0 to 200 meters high outside the initial lake reservoir.

CONCLUSIONS AND FURTHER COMMENTS

A numerical method for the simulation of full three-dimensional free-surface flows has been presented. The proposed computational framework has been successful in solving a variety of test cases (from simple benchmark to real-life situations) with a view to simulating dam breaks. The numerical results show the capability of a full 3D model based on the Navier-Stokes equations, which satisfactorily captures the hyperbolic behavior of water waves while showing non-hydrostatic features that are not present in most reduced models. Such

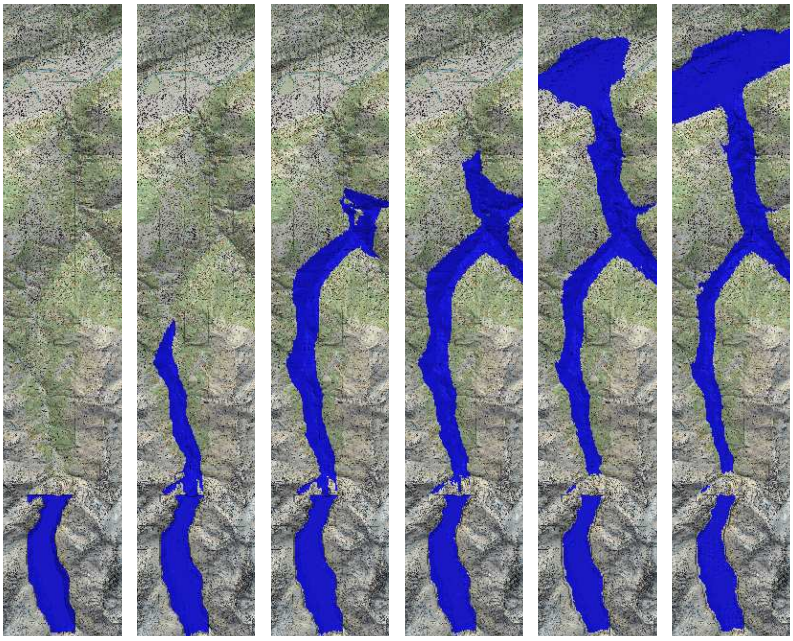

Fig. 13. Numerical solution of the Dixence dam break. Snapshots of the liquid domain (top view) at times $t = 0, 2, 4, 6, 8, 10$ [min].

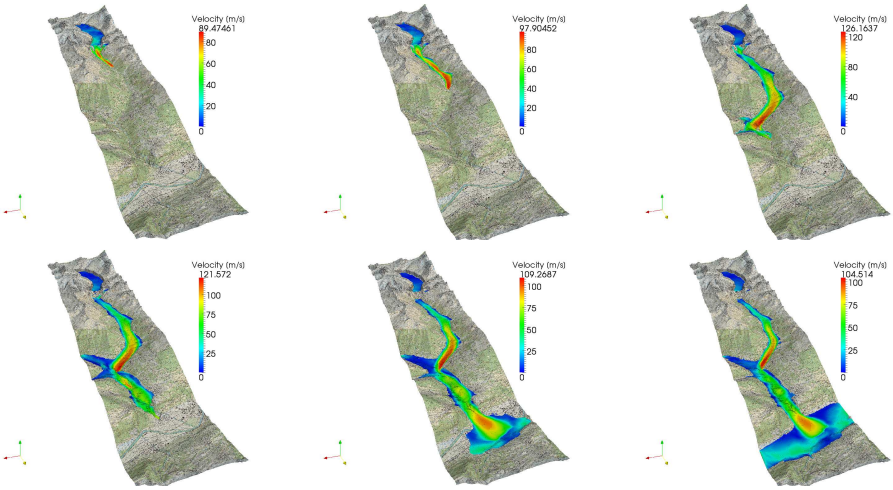

Fig. 14. Numerical solution of the Dixence dam break. Snapshots of the liquid domain with fluid velocity at times $t = 1, 2, 4, 6, 8, 10$ [min].

computational results can thus be very useful to policy makers when delimiting flooding areas and drawing flooding maps, as well as to the hydraulic engineers that are constantly looking for more accurate numerical results of dam break flows (an everlasting major challenge in the hydraulic engineering community). Further work includes the application of the numerical method presented in this article to other practical problems in hydraulic situations on the one hand, such as the modeling and assessment of spillways discharge capacity or that of the sediment transport. The goal is to investigate full 3D effects without additional parametrized effects like friction or turbulence, al-

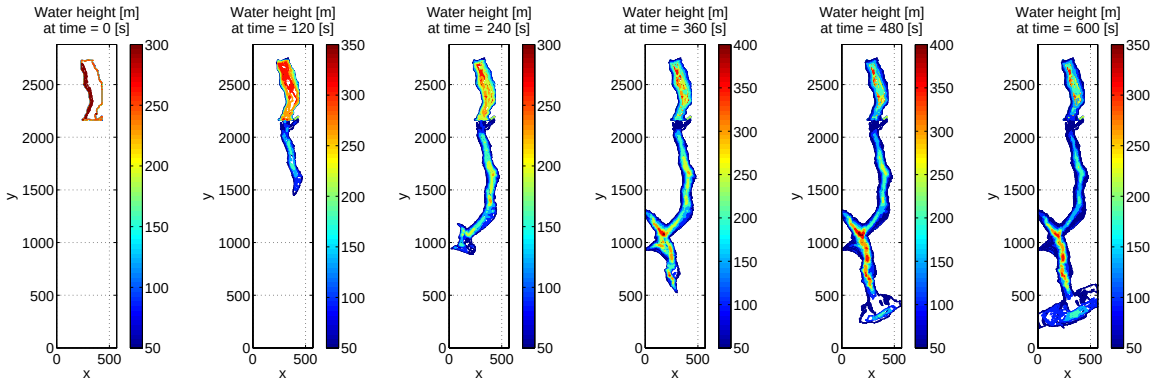

Fig. 15. Numerical solution of the Dixence dam break. Snapshots of the water level (top view) at times $t = 0, 2, 4, 6, 8, 10$ [min].

though they inevitably induce more expensive computational costs as well as more numerical approximations. On the other hand, further work also includes investigations about the sole additional parametrized effects of friction, turbulence, etc.

5 ACKNOWLEDGMENTS

This work was accomplished while SB was a MATHICSE-ASN academic host at EPFL. The authors thank Marco Picasso and Jacques Rappaz (EPFL) for fruitful discussions. SB would like to thank Riadh Ata (EDF R&D), Marie-Odile Bristeau (INRIA) and Nicole Goutal (EDF R&D) for their numerous advice and for providing the 2D mesh for the Malpasset test case.

References

[1] F. Alcrudo and P. Garcia-Navarro. A high-resolution Godunov-type scheme in finite volumes for the two-dimensional shallow-water equations. *Int. J. Numer. Meth. Fluids*, 16:489–505, 1993.

[2] F. Alcrudo and E. Gil. The Malpasset dam break case study. In *Proceedings of the Fourth CADAM Meeting*, pages 95–109, Zaragoza, Spain, 1999.

[3] E. Audusse, M. O. Bristeau, and A. Decoene. 3D free surface flows simulations using a multilayer Saint-Venant model. Comparisons with Navier-Stokes solutions. In Alfredo Berumdez de Castro, Dolores Gomez, Peregrina Quintela, and Pilar Salgado, editors, *Numerical Mathematics and Advanced Applications*, pages 181–189. Springer Berlin Heidelberg, 2006.

[4] C. Biscarini, S. Di Francesco, and P. Manciola. CFD modelling approach for dam break flow studies. *Hydrol. Earth. Syst. Sci.*, 14:705–718, 2010.

[5] Francois Bouchut and Michael Westdickenberg. Gravity driven shallow water models for arbitrary topography. *Commun. Math. Sci.*, 359–389(3), 2004.

[6] A. Caboussat. A numerical method for the simulation of free surface flows with surface tension. *Computers and Fluids*, 35(10):1205–1216, 2006.

[7] A. Caboussat, P. Clausen, and J. Rappaz. Numerical simulation of two-phase flow with interface tracking by adaptive Eulerian grid subdivision. *Math. Comput. Modelling*, to appear, 2011.

[8] A. Caboussat, M. Picasso, and J. Rappaz. Numerical simulation of free surface incompressible liquid flows surrounded by compressible gas. *J. Comput. Phys.*, 203(2):626–649, 2005.

[9] V. Casulli and G. S. Stelling. Semi-implicit subgrid modelling of three-dimensional free-surface flows. *Int. J. Numer. Meth. Fluids.*, 67:441–449, 2011.

[10] V. Casulli and P. Zanolli. Comparing analytical and numerical solution of nonlinear two and three-dimensional hydrostatic flows. *Int. J. Numer. Meth. Fluids.*, 53:1049–1062, 2007.

[11] H. Chanson. Application of the method of characteristics to the dam break wave problem. *J. Hydr. Research*, 47(1):41–49, 2009.

[12] M. Dumbser. A simple two-phase method for the simulation of complex free surface flows. *Comput. Methods Appl. Mech. Engrg.*, 200:1204–1219, 2011.

[13] R. J. Fennema and M. H. Chaudhury. Explicit methods for 2-D transient free-surface flows. *J. Hydr. Engrg*, 116(8):1013–1034, 1990.

[14] S. Soares Frazao, F. Alcrudo, and N. Goutal. Dam-break test cases summary. In *Proceedings of the Fourth CADAM Meeting*, pages 9–25, Zaragoza, Spain, 1999.

[15] D. L. George. Adaptive finite volume methods with well-balanced Riemman solvers for modeling floods in rugged terrain: Application to the Malpasset dam-break flood (France, 1959). *Int. J. Numer. Meth. Fluids*, 66(8):1000–1018, 2011.

[16] J.-F. Gerbeau and B. Perthame. Derivation of viscous Saint-Venant system for laminar shallow water; numerical validation. *Discrete and Continuous Dynamical Systems, Ser. B*, 1(1):89–102, 2001.

[17] R. Glowinski. *Finite Element Method For Incompressible Viscous Flow*, volume IX of *Handbook of Numerical Analysis (P.G. Ciarlet, J.L. Lions eds)*, pages 3–1176. Elsevier, Amsterdam, 2003.

[18] N. Goutal. The Malpasset dam failure. An overview and test case definition. In *Proceedings of the Fourth CADAM Meeting*, pages 1–8, Zaragoza, Spain, 1999.

[19] N. Goutal. Presentation of 1D and 2D simulations of Malpasset dam break wave propagation. In *Proceedings of the Fourth CADAM Meeting*, pages 119–130, Zaragoza, Spain, 1999.

[20] J.-M. Hervouet. *Hydrodynamics of Free Surface Flows: Modelling with the Finite Element Method*. Wiley, London, 2007.

[21] Y. Loukili and A. Soulaïmani. Numerical tracking of shallow water waves by the unstructured finite volume WAF approximation. *Int. J. Computational Methods in Engineering Science and Mechanics*, 8:1–14, 2007.

[22] I. MacDonald, M. J. Baines, N. K. Nichols, and P. G. Samuels. Analytic benchmark solutions for open-channel flows. *J. Hydr. Engrg*, 123(11):1041–1045, 1997.

[23] A. De Maio, F. Savi, and L. Sclafani. Three-dimensional mathematical simulation of dambreak flow. In *Proceeding of IASTED conferences Environmental Modelling and Simulation*, St. Thomas, US Virgin Island, 2004.

[24] F. Marche. Derivation of a new two-dimensional viscous shallow water model with varying topography, bottom friction and capillary effects. *European Journal of Mechanics-B/Fluids*, 26(1):49–63, 2007.

[25] V. Maronnier, M. Picasso, and J. Rappaz. Numerical simulation of three dimensional free surface flows. *Int. J. Num. Meth. Fluids*, 42(7):697–716, 2003.

[26] M. Mohammadi. Boundary shear stress around bridge piers. *Am. J. Appl. Sci.*, 5(11):1546–1550, 2008.

[27] N. Nagata, T. Hosoda, T. Nakato, and Y. Muramoto. Three-dimensional numerical model for flow and bed deformation around river hydraulic. *J. Hydraul. Eng.*, 131:1074–1087, 2005.

[28] I. R. Park, K. S. Kim, J. Kim, and S. H. Van. A volume-of-fluid method for incompressible free surface flows. *Int. J. Numer. Meth. Fluids.*, 61:1331–1362, 2009.

[29] D. Pritchard and A. J. Hogg. On sediment transport under dam-break flow. *J. Fluid Mech.*, 473:265–274, 2002.

[30] A. Ritter. Die fortpflanzung der wasserwellen. *Zeitschrift des Vereins Deutscher Ingenieure*, 36:947–954, 1892.

[31] Y. Shi and K. D. Nguyen. A projection method-based model for dam- and dyke-breaks flows unsing an unstructured finite-volume technique: Applications to the Malpasset dam break (France) and to the flood diversion in the Red River basin (Vietnam). *Int. J. Numer. Meth. Fluids*, 56(8):1505–1512, 2008.

[32] T. Shigematsu, P. L.-F. Liu, and K. Oda. Numerical modeling of the initial stages of dam-break waves. *J. Hydr. Research*, 42(2):183–195, 2004.

[33] J. J. Stoker. *Water Waves: The Mathematical Theory with Applications*. Interscience, London, 1957.

[34] A. Valiani, V. Caleffi, and A. Zanni. Case study: Malpasset dam break simulation using a two-dimensional finite volume method. *J. Hydr. Engrg*, 128(5):460–472, 2002.

Recent publications :

MATHEMATICS INSTITUTE OF COMPUTATIONAL SCIENCE AND ENGINEERING
Section of Mathematics
Ecole Polytechnique Fédérale
CH-1015 Lausanne

01.2012 A. ABDULLE, A. NONNENMACHER:
A posteriori error estimate in quantities of interest for the finite element heterogeneous multiscale method

02.2012 F. NOBILE, M. POZZOLI, C. VERGARA:
Time accurate partitioned algorithms for the solution of fluid-structure interaction problems in haemodynamics

03.2012 T. LASSILA, A. MANZONI, A. QUARTERONI, G. ROZZA:
Boundary control and shape optimization for the robust design of bypass anastomoses under uncertainty

04.2012 D. KRESSNER, C. TOBLER:
htucker – A Matlab toolbox for tensors in hierarchical Tucker format

05.2012 A. ABDULLE, G. VILLMART, KONSTANTINOS C. ZYGALAKIS:
Second weak order explicit stabilized methods for stiff stochastic differential equations.

06.2012 A. CABOUSSAT, S. BOYAVAL, A. MASSEREY:
Three-dimensional simulation of dam break flows.